An alternative mechanism for activation of innate immune signaling by MDA5

Salina Quack[1,2], Sourav Maity[3], Pim P. B. America[1], Misha Klein[1], Alba Herrero del Valle[4,5], Rahul Singh[4,5], Quinte Smitskamp[1], Flavia S. Papini[2], Chase P. Broedersz[1], Wouter H. Roos[3], Yorgo Modis[4,5], and David Dulin[1,2]

[1] Department of Physics and Astronomy, and LaserLaB Amsterdam, Vrije Universiteit Amsterdam, De Boelelaan 1081, 1081 HV, Amsterdam, The Netherlands

[2] Junior Research Group 2, Interdisciplinary Center for Clinical Research, Friedrich-Alexander-University Erlangen-Nürnberg, Cauerstr. 3, 91058 Erlangen, Germany

[3] Moleculaire Biofysica, Zernike Instituut, Rijksuniversiteit Groningen, Groningen, The Netherlands

[4] Molecular Immunity Unit, Department of Medicine, University of Cambridge, MRC Laboratory of Molecular Biology, Francis Crick Avenue, Cambridge CB2 0QH, United Kingdom

[5] Cambridge Institute of Therapeutic Immunology & Infectious Disease (CITIID), Department of Medicine, University of Cambridge, Cambridge CB2 0AW, United Kingdom

Abstract

Long double-stranded (ds) RNA in the cytosol acts as a potent inflammatory molecule recognized by the receptor MDA5, triggering the innate immune response. Mutations in MDA5 affecting dsRNA recognition can lead to increased infection sensitivity or autoimmune disease. The current model proposes that MDA5 nucleoprotein filament assembly-disassembly dynamics regulates long dsRNA recognition and signaling. We show that MDA5 preferentially loads onto dsRNA via a 3' recessed end and uses ATP hydrolysis to translocate towards the 5'-end until obstructed, such as by another MDA5 on the opposite strand. Multiple MDA5 monomers accumulate at the blockade, forming a partial filament that extrudes the associated RNA in single-stranded loops and thereby compacting the MDA5-RNA complex. The compacted state is further stabilized by oligomerization of the MDA5's caspase recruitment domain (CARD) and can withstand significant forces, offering an alternative intermediate in the activation of MDA5-dependent innate immunity.

Introduction

Long double-stranded (ds) RNA is a product of RNA and DNA virus replication (*1*, *2*), and its presence in the cytosol triggers an innate immune response (*3*). Moreover, recent studies have shown that dsRNA may also originate from cellular dysfunctions, and triggers the same innate immune response (*4*, *5*). Recognition of dsRNA in the cytosol is achieved by pattern-recognition receptors, such as the melanoma differentiation-associated gene-5 (MDA5) (*6*). MDA5 is one of the three RIG-I (retinoic acid-inducible gene I)-like receptors that also includes RIG-I, which binds to di- or tri-phosphorylated 5'-ends, and LGP2, which preferentially binds to blunt-ended dsRNA (*6*). MDA5 proofreads RNA in the cytosol to detect and signal in response to virus- or retroelement-derived dsRNA, but generally not structured cellular RNAs (*7*).

MDA5 contains a central RIG-I-like superfamily 2 RNA helicase module flanked by two N-terminal caspase activation and recruitment domains (2CARD) and a C-terminal domain (CTD) (*8*, *9*). The CTD and helicase module associate with the phosphodiester backbone of dsRNA in a ring-like conformation to cooperatively assemble into helical filaments on long (> 500 bp) dsRNA (*8*–*16*). It has been proposed that filament assembly plays a central role in recognition and proofreading, through a competition between cooperative assembly and ATP-hydrolysis dependent dissociation, enabling the selection of dsRNAs longer than 500 bp (*11*, *12*, *17*). In addition, structural studies have shown that conformational changes coupled to ATP hydrolysis, including an increase in MDA5 footprint on dsRNA from 14 to 15 bp, confer a mechanical proofreading activity, thereby promoting dissociation from imperfectly base-paired RNAs (*8*, *9*) (**Figure 1A**). The increase in filament footprint from consecutive rounds of ATP hydrolysis by adjacent MDA5s can displace tightly bound proteins from dsRNA (*18*, *19*). Furthermore, ATP hydrolysis also enables MDA5 monomer long range translocation on dsRNA (*20*). Following the ATP hydrolysis step, the 2CARDs from the MDA5 filament oligomerize (*12*, *14*) and the resulting oligomer thereafter nucleates the helical fibril formation at the mitochondrial outer membrane through association with the CARD domain of the mitochondrial antiviral signaling (MAVS) proteins (*21*, *22*). The MAVS CARD oligomers subsequently activate antiviral interferon responses (*16*, *21*, *23*), which also results in a positive feedback loop that increases MDA5 expression and its intra-cytosolic concentration (*24*–*26*).

Mutations in the gene encoding MDA5 that compromise its proofreading ability have been linked to interferonopathies (*27*, *28*), including Aicardi-Goutières syndrome (*29*–*31*), and Singleton-Merten syndrome (*32*). These pathogenic mutations often alter the ATPase activity of MDA5's helicase domain, indicating its central role in dsRNA recognition and proofreading. The MDA5 ATPase activity is dependent on dsRNA binding and is tightly regulated efficient and accurate dsRNA recognition. Indeed, the gain-of-function mutant R338G MDA5 (mouse MDA5, R337G in human) has only 5% of the ATPase activity of WT MDA5 leading to increased stability of MDA5-dsRNA signaling complexes due to reduced dissociation of MDA5 from dsRNA (*31*). Conversely, the loss-of-function mutant I923V (*11*, *33*) is ATPase hyperactive and forms less stable filaments. Although the initial steps in RNA recognition by MDA5 have been studied in detail, key questions remain regarding how MDA5 filaments bound to dsRNA assemble into active signaling complexes, in particular how MDA5 discriminates long dsRNAs from shorter ones. To understand how MDA5 filament formation and ATP hydrolysis lead to the formation of signaling complexes, high resolution and real-time data monitoring of this process on single long dsRNA molecules are needed.

Here, we employed high-throughput single-molecule magnetic tweezers and high-speed AFM to investigate the mechanism of dsRNA recognition by MDA5. We confirm that, in absence of ATP, MDA5 filament formation on dsRNA is cooperative and rate-limited by a slow nucleation step. Furthermore, MDA5 underwinds dsRNA upon binding. In the presence of ATP, MDA5 loads on dsRNA more efficiently via a recessed 3'-end than internally. In absence of any obstacle, MDA5 translocates until running off a 5'-end. When the RNA 5'-end is blocked or MDA5 encounters an obstacle, MDA5 forms a partial filament and utilizes ATP hydrolysis to unwind and compact the dsRNA tether by extruding single-stranded RNA loops, even against 4 pN opposing force. The loop-extruded MDA5-RNA complex is further stabilized and compacted by CARD-CARD interactions and requires forces as large as than 20 pN to break apart, providing another pathway to neutralize viral dsRNA. This study provides a comprehensive mechanism for how MDA5 recognizes and neutralizes long dsRNA to form a signaling complex.

Results

A single-molecule magnetic tweezers assay to monitor MDA5 filament formation on long dsRNA.

We established a high-throughput magnetic tweezers assay to investigate the assembly and mechanochemical properties of MDA5 filaments on long dsRNA (*34–36*). Here, a magnetic bead was tethered to the surface of the bottom coverslip of a flow chamber via a ~3.2 kbp long dsRNA (**Figure 1B**) (*37*). The tether was flanked by two handles, one with multiple biotin molecules to attach to the streptavidin-coated magnetic bead, and one with multiple digoxygenin molecules to bind to the anti-digoxigenin coated glass surface of the flow chamber (**Materials and Methods**) (*37*). Several attachment points at both ends rendered the dsRNA tether coilable (*38*, *39*) (**Materials and Methods**). A pair of permanent magnets located above the flow chamber applied an attractive force and constrained the rotation of the magnetic bead (*34*, *36*, *37*) (**Materials and Methods**). Hundreds of magnetic beads were imaged simultaneously on a large chip CMOS camera via a home-built inverted microscope. Bead positions in three dimensions were estimated in real-time with nanometer resolution using a custom LabVIEW interface (*40*). The extension of the tether as a function of force was measured by continuously varying the distance between the magnets and the magnetic bead (*41*). These experiments are coined 'force-extension experiments' and were performed on either bare dsRNA or MDA5 filaments. Around 40% of the dsRNA tethers monitored in the flow chamber were coilable and were used to perform torque-dependent investigations of either bare dsRNA or MDA5-filaments during rotation-extension experiments. Here, the torque applied to the magnetic beads is used to transfer any amount of positive or negative turns applied to the magnets into the RNA while measuring the extension of the tether (*38*, *42–44*).

MDA5 assembles directionally and cooperatively into stiff and stable filaments in absence of ATP.

We investigated MDA5 filament formation and its mechanical properties under force using either a non-hydrolysable form of ATP (AMP-PNP) (**Figure 1CD**) or the product of ATP hydrolysis (ADP) (**Figure S1A**). Before adding MDA5 to the flow chamber, the coilability of the dsRNA tethers was determined by performing a rotation-extension experiments at ~4 pN force. Coilable dsRNA tethers showed a decrease in extension only when positive turns are added (**Figure S1B**), consistent with previous measurements (*42*). Thereafter the force was adjusted to 0.1 pN to maximize the change in tether extension upon filament formation. Furthermore, at such force, the dsRNA tether is only stretched ~50% of its contour length ($L_C = 900\ nm$), and conformational fluctuations of the tether are sufficiently large to occasionally bring distant sections of the filament in contact. After injecting

MDA5 into the flow chamber and a subsequent nucleation time, non-coilable and coilable tethers showed an initial increase in extension, indicating the formation of a MDA5 filament. This was followed by either a stable extension of the former (**Figure 1C**) or a rapid decrease in extension of the latter (**Figure 1D**).

Focusing on the non-coilable tethers first (**Figure 1C**), we extracted the MDA5 filament nucleation rate and the filament formation rate as a function of MDA5 concentration (**Figure S1C** and **Figure S1D**, respectively). If MDA5 binding to the RNA was limiting the nucleation reaction, and assuming that the MDA5 concentration in the flow cell remains constant during the experiment, we should have expected a monotonic increase in the nucleation rate with MDA5 concentration. However, upon varying the MDA5 concentration from 25 to 300 nM, we found that the nucleation rate increased from (0.010 ± 0.001) s^{-1} to (0.062 ± 0.010) s^{-1} (mean rate ± standard deviation) and saturated above 150 nM (**Figure S1C**, **Table S1**). We confirmed this observed saturation was not the result of an increasing number of nucleation events occurring during the flush of the proteins into the flow cell. For these traces, we only confirmed the formation of a filament subsequently and could not record a nucleation rate. Yet, the relative number of formed filaments for which we could determine the nucleation event did not drop below ~40 % (**Figure S1E**). This confirmed that the nucleation rate was independent of MDA5 concentration beyond 150 nM, at which point it was limited by a process other than binding to the dsRNA, e.g. accommodating dsRNA into MDA5. We next defined the filament formation rate as the average of the local slope of the tether extension obtained from a sliding window (**Material and Methods**). MDA5 filaments formed at a rate that increased exponentially with concentration, i.e. from (0.7 ± 0.1) monomers/s to (8 ± 1) monomer/s (mean rate ± standard deviation, assuming a 14 bp footprint per MDA5 monomer (*8*, *9*)) at 25 and 300 nM MDA5 respectively (**Figure S1D**, **Table S1**). The filament formation rate was significantly larger than the nucleation rate, supporting a cooperative MDA5 filament formation (*45*), in agreement with previous reports (*11*, *12*, *15*).

We performed dynamic force-extension measurements to characterize the mechanical properties of the filament under force, first on the bare dsRNA tether preceding MDA5 injection into the flow chamber, and on the same tether after the MDA5-filament's extension levelled off (**Figure 1E**, **Figure S1F-N**) (*41*). We fitted the inextensible worm-like chain model (*46*) to the dynamic force-extension traces (**Materials and Methods**), extracting a contour length L_C and a persistence length L_P for every tether (**Figure S1OP**, **Table S2**). The dsRNA force-extension data were consistent with previous measurements performed in a buffer containing magnesium, i.e. $L_C = 900\,nm$ and $L_P = 45\,nm$ (**Figure S1OP, Table S2**) (*42*, *47*). The filaments exhibited a contour length similar to dsRNA (**Figure 1E, Figure S1O**, **Table S2**), while the persistence length increased by ~3-fold, i.e. up to ~160 nm (**Figure S1P**, **Table S2**). We subsequently tested the stability of MDA5 filaments in the absence of ATP hydrolysis, we flushed out excess MDA5 proteins with a reaction buffer containing 2 mM of either AMP-PNP or ADP. We subsequently performed force-extension experiments every 30 min for up to two hours (**Figure S2AB**). As the filament force-extension behaviors remain largely unchanged over time, we therefore concluded that MDA5 forms stable filaments in standard reaction buffer with either AMP-PNP or ADP (**Figure S2AB, Table S3**). In absence of adenosine MDA5 could form filaments that disassembled over time. This is evidenced by force-extension traces taken at later time points aligning with the bare dsRNA force-extension trace (**Figure S2C, Table S3**). Adding 0.7 M NaCl in the reaction buffer also resulted in filament disassembly (**Figure S2D, Table S3**). Furthermore, the MDA5-

dsRNA filaments could withstand forces up to ~50 pN in standard reaction buffer with ADP (**Figure S2E**). Overall, at physiological ionic strengths and in the presence of ADP or AMP-PNP, the filaments were stable.

To further elaborate on MDA5 binding affinity to dsRNA and cooperative assembly into filaments, we fitted a Hill model to the fractional occupancy α extracted from the increase in persistence length of the tether as a function of MDA5 concentration (*48*) (**Materials and Methods**):

$$\alpha([MDA5]) = \frac{[MDA5]^n}{{K_D}^n + [MDA5]^n} \quad (1),$$

with K_D being the apparent dissociation constant, [MDA5] being the concentration of MDA5, and n being the Hill coefficient to the fractional occupancy. For wild-type MDA5, we measured $K_D = (34 \pm 14)\, nM$ and $n = (2.2 \pm 1.8)$ (**Figure 1J**), which confirms a cooperative assembly of MDA5 filament ($n > 1$) (*11*, *12*, *15*, *17*). Increasing the force to 1 pN lowered the noise in the traces and pauses became apparent during the filament formation (**Figure S2F**). If a filament can grow only in one direction, it would grow until reaching an obstacle, e.g. another filament extremity or an attachment point. Further growth would then only be possible if another (slow) nucleation event occurred, resulting in a pause in the tether extension increase. We therefore interpret the pause we observed as a unidirectional filament formation (**Figure S2F**), in line with previous reports (*17*).

MDA5 underwinds dsRNA upon binding in absence of ATP hydrolysis

We next investigated the torsional properties of the MDA5-dsRNA filament by performing rotation-extension experiments at different forces in the presence of ADP (**Figure S3A-D**). The MDA5 filament rotation-extension was strongly asymmetric for forces up to 2 pN (**Figure S3A**), i.e. a rapid decrease in extension upon positive supercoiling, but a slow decrease in extension upon negative supercoiling (**Figure S3B**). Above 4 pN the rotation-extension curves were symmetric. The rotation rate for negative supercoils is largely force independent at ~1 nm/turn. In contrast, upon positive supercoiling the rate decreased from (15 ± 2) nm/turn to (0.74 ± 0.06) nm/turn when increasing the force from 0.1 to 8 pN, respectively (**Figure S3C, Table S4**). We observed that filaments assembled on non-coilable dsRNA tethers became thereafter coilable, which suggests that MDA5 monomers can bridge over the nick(s) in the dsRNA backbone (**Figure S3D**).

Following MDA5 filament nucleation on coilable tethers, the initial tether length increased (**Figure 1D, Figure S3E**). However, the filament formation was ~10 times slower and the maximum extension reached by the filament was significantly shorter than for non-coilable dsRNA (**Figure S3F, Table S5**). Subsequently, the tethers compacted at a rate of ~5 nm/s (**Figure S3F**). All the tethers eventually reached a minimum extension, leading to a tight and irreversibly compacted form recognizable by its significant reduction in the z-axis fluctuation of the bead position (**Figure S3GH**). The compacted state could withstand forces up to 8 pN (**Figure 1E**). Given the difference with non-coilable tethers (**Figure 1C**, **Figure S1A**), we hypothesized that the compaction phase observed with coilable tethers originated from dsRNA being either overwound or underwound upon MDA5 binding. In the former case, the tether would present no single-stranded (ss) RNA region and therefore be insensitive to RNase A (**Figure S3IJ**). In the latter case, the dsRNA region of the tether that are not covered by MDA5 filament would melt at forces above 1 pN (*42*) (**Figure S1B**, **Figure S3I**), rendering them sensitive to cleavage by RNase A (**Figure S3K**). MDA5 protects dsRNA against RNase degradation (*49*), and only the free dsRNA gap, unwound when negatively supercoiled, would be accessible to

RNase A. To this end, we performed rotation-extension experiments on MDA5-dsRNA filaments before and after flushing RNase A into the flow chamber, while keeping the force at 4 pN throughout the experiment (**Figure 1G**). The addition of RNase A in the flow chamber resulted in the loss of coilability of the tethers (**Figure 1H**). We therefore conclude that MDA5 underwinds dsRNA in the absence of ATP hydrolysis.

ATP-hydrolysis induces MDA5 filament compaction stabilized by CARD-CARD interactions.

To evaluate how ATP hydrolysis impacts the structural organization of a filament, we pre-assembled the filament in the presence of ADP and subsequently introduced a buffer containing ATP into the flow chamber (**Figure 2AB**). We immediately noticed a decrease in extension of the tethers after injecting ATP (**Figure 2B**). We coined this phase 'compaction'. The traces also showed abrupt increases in the trace – coined 'rupture' events – during the compaction phase (at ~200 s and ~300 s in **Figure 2B**). The compacted filament formed in presence of ATP were very stable, withstanding forces up to $(20 \pm 4)\ pN$ (mean ± standard deviation) (**Figure S2A**).

We noticed that the compaction rate increased exponentially with increasing concentration of ATP (**Figure S4B, Table S6**) and decreased with force (**Figure S4C**, **Table S6**). Furthermore, we observed many rupture events at decreasing force and increasing ATP concentration, i.e. where the tether extension suddenly increased after a compaction phase (**Figure S4DE, Table S6**). However, such events did not occur once the filament was compacted (**Figure S4D**). We propose that MDA5 protomers located far from each other within an MDA5 filament can become apposed during the compaction phase due to thermal motion. These fluctuations enable intermolecular CARD-CARD interactions, with occasional failures seen as rupture events, but eventually leading to a stable compacted state. Consistent with this model, at higher applied forces, when the tether is nearly straightened, we see a general decrease in the number of rupture events seen per trace (**Figure S4E**). At higher ATP concentrations we observed more rupture events per trace (**Figure S4E**), indicating that ATPase activity of MDA5 promotes long distance intermolecular CARD-CARD interactions. In conclusion, MDA5 can compact a filament against a significant force through ATP hydrolysis and CARD-CARD interactions stabilize the resulting compacted filament.

Next, we deployed high-speed atomic force microscopy (HS-AFM) studies (*50*, *51*) to visualize the MDA5 interactions on dsRNA upon ATP hydrolysis. We pre-assembled MDA5-dsRNA filaments in presence of 2 mM ADP in solution and subsequently adsorbed them on a mica surface. We could clearly identify the MDA5 monomers on a dsRNA strand (**Figure S4F**) and imaged the complex over time (**Figure S4G**). After ~124 s, 6 mM ATP was added (**Video S1**), resulting in translocation and compaction of the MDA5-dsRNA filament (**Figure 2C, Video S1**).

To test our model of CARD-dependent filament compaction, we investigated two clinically relevant MDA5 mutants, R338G and I923V, and a mutant without 2CARD (ΔCARD). MDA5 ATPase-dead mutant R338G (**Figure 1A**) is a pathological gain-of-function mutant that increases signaling and interferon production (*31*). The filaments formed by the R338G MDA5 mutant in the presence of ADP had the same mechanical properties as the ones formed with wild-type (WT) MDA5. They showed similar persistence and contour lengths (**Figure S5A, Table S7**), underwound coilable dsRNA upon binding (**Figure S5B**) and had a similar rotation-extension behavior as wild-type MDA5 (**Figure S5C**). Removing ADP and excess proteins followed by the addition of 4 mM ATP was neither followed by a

decrease of the tether extension (**Figure 2D**), nor MDA5 R338G dissociation from the dsRNA tether. The subsequent force-extension analysis provided similar persistence and contour lengths as preceding ATP addition (inset **Figure 2D**, **Figure S5A**, **Table S7**). ATP hydrolysis is therefore essential for either MDA5 filament compaction or dissociation.

We next investigated the ATPase hyperactive variant I923V (**Figure 1A**). MDA5 I923V has a 2-fold greater ATPase activity (*33*) and a loss of antiviral signaling activity relative to WT MDA5 (*11*, *33*, *52*). The MDA5 I923V filaments had similar persistence and contour lengths in the presence of ADP as WT MDA5 filament (**Figure S5D, Table S7**) and underwound dsRNA upon binding on a coilable tether (**Figure S5E**). However, rotating the magnetic bead from negative to positive turns resulted in a complete dissociation of the I923V mutant filament (**Figure S5F**), indicating that this filament was unstable under torsional stress. Interestingly, addition of either low or high ATP concentration resulted in two very different responses from the I923V MDA5 filament (**Figure 2EF**). At low ATP concentration (0.5 mM), we observed the dissociation of MDA5 from dsRNA (**Figure 2E**), confirmed by the subsequent force-extension measurement (inset **Figure 2E**, **Table S7**). However, at high ATP concentration (4 mM), the filament compacted into a stable and tight complex (**Figure 2F**), similarly to WT MDA5 filament (**Figure 2B**). Together, these results support a two-step ATP dependent model for compaction, e.g. MDA5 binding is destabilized by ATP hydrolysis (*8*, *9*), followed by either rapid binding of another ATP molecule to enable the next hydrolysis cycle or MDA5 dissociation from dsRNA. A mutant such as MDA5 I923V therefore requires higher ATP concentration to compensate the binding instability due to the mutation.

Finally, we investigated how 2CARD impacted the filament compaction with the MDA5 ΔCARD mutant. 2CARD constitutes the N-terminus of MDA5 (**Figure 1A**) and form stable interactions with the CARD of MAVS. This association is essential to promote immune response signaling (*53*). Furthermore, 2CARD have been proposed to play another important role in connecting neighboring MDA5's within the filament (*14*). MDA5 ΔCARD formed a filament on dsRNA with comparable L_C and L_P as the WT MDA5 filament (**Figure S5G**, **Table S7**) (*12*). Association of MDA5 ΔCARD to a coilable dsRNA led to underwinding, similarly to WT MDA5 (**Figure S5H**). However, rotation-extension experiments on a filament formed on a non-coilable dsRNA showed no change in extension in the absence of ATP, unlike WT MDA5 (**Figure S5I**). This result suggests that 2CARD bridges consecutive MDA5 protomers in the filament rendering a non-coilable dsRNA tether coilable (**Figure S3D**). Upon addition of ATP into the flow chamber, MDA5 ΔCARD dissociated from the dsRNA (**Figure 2G**), as confirmed by the consecutive force-extension experiment (inset **Figure 2G**, **Table S7**). Therefore, in addition to stabilizing MDA5 filaments by connecting adjacent (or nearby) protomers, we identified a new role for 2CARD in dsRNA compaction.

Full MDA5 filament assembly is not required for dsRNA compaction.

All experiments until now were performed in two steps: first filament formation in absence of ATP, followed by flushing out all excess proteins and injection of reaction buffer with ATP. While these experiments enabled the separate monitoring of filament assembly and ATP-hydrolysis dependent compaction, such conditions are not physiological. We therefore performed experiments where we monitored MDA5 filament assembly and compaction with 1 mM ATP continuously present (**Figure 3A-C**, **Figure S6A-E**). We focused on non-coilable dsRNA to circumvent potentially misinterpreting compaction events as the result of dsRNA supercoiling (**Figure 1K-L**). At low MDA5 concentration (50

nM) and low force (0.1 pN), the filament slowly nucleated, as expected (**Figure 3B**), and started to form a filament, as noticeable by the increase in the tether's extension (**Figure 3B, Figure S6E**). However, unlike the ~350 nm increase in extension we would have expected for a full filament formation (**Figure 1C**), we only monitored a ~100 nm increase in extension preceding compaction (**Figure 3B**). This indicates that a partial filament is sufficient to enable compaction. On the other hand, at high MDA5 concentration (400 nM), the filament reached near completion, i.e. ~300 nm increase in tether extension, often during the flush, followed by rapid compaction (**Figure 3C**). We then performed the same experiments at high force (1 pN), to prevent long distance CARD-CARD interactions during tether compaction. At low MDA5 concentration (50 nM), the tether extension remained largely constant upon addition of MDA5 until compaction started (~1700 s) (**Figure S6D**), further confirming that compaction did not necessitate full filament formation. At higher MDA5 concentration (400 nM), we noticed that most filaments completed assembly while the proteins were being flushed into the flow chamber, rapidly followed by compaction (**Figure S6E**). As in the presence of ATP the nucleation time could not be reported, we now evaluate the time preceding MDA5 filament compaction referred to as the pre-compaction rate. It increases with MDA5 concentration from $(0.0032 \pm 0.0004)\ s^{-1}$ to $(0.016 \pm 0.003)\ s^{-1}$ for MDA5 concentration varying from 25 to 400 nM, respectively, showing a saturation above 100 nM (**Figure 3D**). Compaction rates for filaments formed in the presence of ATP were roughly 2- to 3-fold greater than for the filaments pre-formed in the presence of AMP-PNP/ADP and independent of MDA5 concentration (**Figure 3E**, **Figure S6F**, **Table S8**).

MDA5 loads faster onto dsRNA at recessed 3'-ends than internally and compaction is not due to supercoiling.

MDA5 filament assembly renders a non-coilable dsRNA coilable (**Figure S3D**). Structural studies support a change in dsRNA twist induced by MDA5 during the ATP hydrolysis cycle (*8*, *9*). Therefore, the filament compaction could originate from plectoneme formation due to a change in dsRNA twist (*36*). To test this hypothesis, we inserted a 30 nt ssRNA gap near either the 3'-end or the 5'-end of the RNA strand annealed to the tethering strand, preceding either the biotin- or digoxygenin-labeled handle, and coined these constructs 3'-gap and 5'-gap up strand (based on MDA5 translocation direction, see following paragraph), respectively (**Figure 4AC, Materials and Methods**). As MDA5 does not bind to ssRNA (*54*), such constructs allow for two separate filament fragments to form (on either side of the gap) that cannot be bridged by MDA5. Hence, the tether would remain non-coilable. Experiments were performed at 1 pN to prevent long distance CARD-CARD interactions that could make the tether coilable. Interestingly, upon addition of 50 nM MDA5 and 1 mM ATP, we observed a similar reaction for both gapped constructs as without gap (**Figure S6D**), i.e. a rapid tether compaction into stable, tight complexes (**Figure 4BD**), as reported by the subsequent force-extension experiment (**Figure 4BD**, insets). Furthermore, we did not observe any increase in extension upon addition of MDA5, i.e. compaction occurred without having a visible filament formation, further indicating that filament completion is not required for compaction (**Figure 4BD**).

To rule out any bias in the orientation of the gap in either RNA strand, we designed an RNA construct with a 5'-gap in the 'down' strand (**Figure S7A**) or in both strands (**Figure S7B**). Both constructs showed a similar behavior as the constructs with gaps in the up strand only (**Figure 4BD**).

Interestingly, we measured a ~2-fold larger pre-compaction rate for the 3'-gap construct than for any construct with a 5'-gap or dsRNA (**Figure 4E, Table S10**). This result suggests two modes of

MDA5 loading onto dsRNA: either by binding directly to dsRNA or at the 3'-end of one of the two RNA strands when a 5'-overhang is present, the latter being significantly faster (**Figure 4E**). In conclusion, MDA5 filament compaction are not due to supercoiling of either the dsRNA or the filament, and a recessed 3'-end enables faster MDA5 loading in comparison to dsRNA loading.

MDA5 translocates 3' to 5' on dsRNA.

Repeating the experiments on either the 3'- or 5'-gap constructs with high concentration of MDA5 (400 nM, 1 mM ATP), we observed different behaviors (**Figure 5A-D**). While the 3'-gap construct led to the same reaction as without a gap (**Figure S6E**), i.e. a rapid filament assembly – mostly during the flush – followed by compaction (**Figure 5B**), the 5'-gap did not report compaction, but rather a complete filament formation (**Figure 5D**). We hypothesized that MDA5 translocated and ran off the 5'-end preceding the gap. To test our hypothesis, we initially flushed MDA5 with ATP into the flow cell with either the 3' or the 5' gap construct. After ~600 s, we flushed out the MDA5 in excess with a reaction buffer containing ATP (**Figure 5FG**). The 3'-gap tethers rapidly showed compaction (**Figure 5F**), while only $(22 \pm 7)\%$ (mean ± standard deviation) of the 5'-gap tethers demonstrated a similar behavior (bottom trace in **Figure 5G**; **Table S11**). All the other 5'-gap tethers showed complete dissociation of the filament, as reported by the force-extension measurement at the end of the experiment, either progressively or through successive compaction-rupture cycles (top and middle traces, respectively, **Figure 5G**). Placing the 5'-gap in the other strand of the dsRNA tether resulted in the same ratio of filaments compacting over dissociating ($(28 \pm 6)\%$) (**Figure 5H, Figure S8A, Table S11**). We concluded from these experiments that MDA5 translocates 3' to 5' and eventually dissociates when reaching a ssRNA gap region at the 5'-end. From the traces reporting progressive MDA5 dissociation, we could extract a translocation rate for MDA5 of $(5.7 \pm 1.2)\ bp/s$ (mean ± standard deviation, **Table S11**), i.e. similar to the $(8.8 \pm 3.7)\ bp/s$ recently measured using single-molecule fluorescence (*20*).

For the ~25% of the 5'-gap tethers that compacted, we hypothesized that MDA5 could load internally on the opposite strand of the RNA, though less efficiently, and translocate on the strand opposite to the gapped one, towards the magnetic bead located at the 5'-end. It eventually would collide with either the MDA5 translocating on the gapped strand or the magnetic bead attachment, resulting compaction. To verify this hypothesis, we repeated the experiments discussed above with a dsRNA tether containing a 5'-gap in both strands (**Figure S8B**). The fraction of tethers showing compaction after replacing the MDA5 with buffer containing only 1 mM ATP dropped to $(5 \pm 3)\%$ (mean ± standard deviation) (**Figure 5H, Table S11**), supporting our hypothesis.

MDA5 compacts the tether through a dsRNA unwinding mechanism.

We next interrogated the mechanism by which MDA5 compacted the dsRNA tether. From the gapped dsRNA constructs (**Figure 4** and **Figure 5**), we showed that compaction is not due to either dsRNA or filament supercoiling. Furthermore, both gapped constructs compacted at low MDA5 concentration and without forming a filament over the entire dsRNA tether (**Figure 4A-D**). At high MDA5 concentration, the 5'-gap constructs enabled MDA5 run-off dissociation, indicating translocation in the 3' to 5' direction (**Figure 5D-G**). We hypothesized that compaction occurred when a translocating MDA5 collided either head-to-head with another MDA5 translocating on the opposite strand or to an obstacle at either 5'-end, which could be either the glass surface or the magnetic bead. Following the collision, MDA5 was stalled and could not move forward any further, and the work

resulting from ATP hydrolysis was used to unwind dsRNA, bringing both ends of the tether towards each other. This process likely resulted in ssRNA loop extrusion and decreased the extension of the tether.

To test this hypothesis, we partially assembled MDA5 filaments on coilable dsRNAs at 1 pN and with ADP. We used large magnetic beads (2.8 µm diameter, **Materials and Methods**) to apply a force high enough to break the tightly compacted complex (**Figure 2B**). The excess proteins were subsequently flushed out and the magnets removed to let the tether relax any torsional stress (**Figure 6A**). The magnets were mounted back, adjusted to apply a 1 pN force, and ATP was added. Once the tethers were fully compacted, the flow cell was treated with RNase A, and subsequently rinsed with reaction buffer without proteins. High force was applied to break apart the compacted complex, followed by a rotation-extension experiment (**Figure 6AB**). The addition of RNase A to a compacted MDA5 filament rendered the tether non-coilable, confirming the partial conversion of the dsRNA tether into ssRNA following ATP-dependent compaction (**Figure 6B, Table S12**). In absence of either the compaction step, i.e. without ATP (**Figure 6C, Table S12**) or RNAse A (**Figure 6D, Table S12**), the tethers remained coilable. HS-AFM further confirmed that MDA5 converted the dsRNA (**Figure S9A**) into ssRNA (**Figure S9B, Video S2**) in the presence of ATP and when no obstacle was present at either 5'-end of the dsRNA.

Discussion

MDA5 plays a crucial role in sensing and recognizing viral dsRNA from the many structured RNAs present in the cell cytoplasm. To this end, MDA5 binds dsRNA and utilizes ATP hydrolysis to mechanically proofread dsRNA. Previous biochemical ensemble experiments concluded that ATP hydrolysis promoted dissociation of MDA5 from RNA and that such dissociation was further stimulated by high ATP concentrations (*11*, *12*, *14*, *17*). How does the MDA5-dsRNA complex go on to form a signaling complex after repeated cycles of ATP hydrolysis? To answer this question, we employed single-molecule magnetic tweezers and high-speed AFM to physically manipulate and image single dsRNA molecule in interaction with MDA5, as well as monitor how wild-type and mutant MDA5s interact with such a dsRNA in the presence of either ATP or non-hydrolysable analogs.

Based on our experimental investigations, we propose an alternative mechanism for dsRNA recognition and signaling by MDA5 (**Figure 7**). At low MDA5 concentrations (50 nM), MDA5 loads onto dsRNA more efficiently via a recessed 3'-end than internally (**Figure 4E**). This ability may be useful to detect very low amount of viral dsRNA, as for arenavirus that generate very small quantity of one nucleotide 5'-overhang dsRNA (*31*, *55*), which triggers RIG-I and MDA5 signaling in absence of the 5' to 3' exonuclease encoded in the viral genome (*56*). Following loading, MDA5 translocates towards the 5'-end (**Figure 5G**), until it collides with either another MDA5 translocating on the opposite strand, or with an obstacle located downstream the translocation direction. Once several MDA5s have loaded and assembled into a partial filament at the blockade point (**Figure 3B**), the MDA5s' CARD domain oligomerizes and subsequent ATP hydrolysis cycles leads to compaction of the MDA5-RNA complex (**Figure 3-5**). Interestingly, ATP hydrolysis by MDA5 generates sufficient work to compact the MDA5-RNA complex against forces as high as 4 pN (**Figure S4A-D**), which may explain how MDA5 can dislodge proteins tightly bound to dsRNA (*18*, *33*). Compaction occurs via simultaneous dsRNA unwinding and ssRNA loop extrusion (**Figure 6AB**) and is likely facilitated by the initial dsRNA underwinding upon MDA5 binding (**Figure 1DKL**). This process goes on until all bare dsRNA has been pulled through the

MDA5s against the next obstacle. In our assay, such obstacle can be either the magnetic bead and the glass surface attachment points, or another MDA5-MDA5 stalled complex (**Figure 3B, Figure S6D**). In the cellular context, we propose that LGP2 performs such a role when bound to the dsRNA either internally (*19*, *57*) or at the dsRNA ends (*10*, *58*) (**Figure 7**). Indeed, LGP2 binding to dsRNA potentiates MDA5 signaling (*19*, *26*, *59–62*). In the absence of an obstacle at the dsRNA end, MDA5 unwinds the dsRNA completely and eventually falls off from the 5'-ends (**Figure S8B, Video S2**). As a result, no signal is being triggered. Our model is further supported by a recent single-molecule fluorescence study showing that LGP2 blocks MDA5 translocation along dsRNA (*20*). Moreover, in absence of a stretching force, conformational dsRNA chain fluctuations enable long distance CARD-CARD interactions to lock together distant stalled complexes on the same or different dsRNA. This further promotes rapid compaction (**Figure 2B, Figure S4A**). The resulting MDA5-RNA complex is extremely stable, stabilized by CARD-CARD interactions, to the extent that breaking them apart when pulling on compacted filaments resulted in the removal of most MDA5s from dsRNA (insert in **Figure 2B, Figure S4A**). We propose that MDA5 helicase activity is impaired once the filament has fully compacted, due to CARD-CARD oligomerization (**Figure 7**).

At high MDA5 concentrations (400 nM), MDA5 loads on dsRNA internally and onto a recessed 3'-end with the same efficiency (**Figure 5E**). MDA5 filament formation is rate-limited by nucleation in absence of ATP, even at high MDA5 concentrations (**Figure 1E, Figure S1C**), suggesting that a conformational change, e.g. accommodation of dsRNA (**Figure 1KL**), must occur to stabilize the binding. On the other hand, the filament formation rate increases exponentially with MDA5 concentration (**Figure 1F**). This indicates that cooperative MDA5 filament formation dominates the reaction at high MDA5 concentrations (*8*, *11*, *17*), leading to rapid filament growth immediately after the first nucleation event (**Figure 3C**, **Figure 5BF, Figure S6E**). In absence of head-to-head MDA5 collisions, the presence of LGP2, either within or at the dsRNA end, would prevent the filament from falling off the dsRNA, enabling a tight compaction of the MDA5-RNA complex via ssRNA loop extrusion (**Figure 3CE**). At high MDA5 concentration, more than one nucleation event may occur on either strand of the dsRNA, leading eventually leading to collision and compaction (**Figure 5G**). However, the very cooperative filament formation significantly reduces the likelihood of this event at such high MDA5 concentration (**Figure 5D**).

Our work reveals that MDA5 employs ATP hydrolysis to unwind and compact dsRNA into a stable MDA5-RNA complex (**Figure 2B**, **Figure S4A**, **Figure 7**). We propose this tightly compacted form to play an important role in activating signaling. Aggregation of MAVS via CARD-CARD interactions is essential in MDA5 signaling (*13*) and only oligomerized 2CARD can activate MAVS (*14*). Our data shows that CARD-CARD association occurs between neighboring WT MDA5 in absence of ATP hydrolysis, as non-coilable tethers were rendered coilable after WT MDA5 filament fully assembled (**Figure S3D**), but never with MDA5 ΔCARD filaments (**Figure S5I**). However, the filament was stable in absence of ATP and did not self-compact. ATP hydrolysis enabled filament compaction into a tight complex, likely by through loop extrusion increasing the local concentration of MDA5 2CARDs and hence promoting oligomerization of 2CARDs bound to non-adjacent sequences on the RNA. The stability of the MDA5-RNA complex after compaction (**Figure 2B**) suggests that it plays an essential role in capturing viral dsRNA, i.e. making them thereby unavailable for viral replication, while simultaneously ensuring an effective signaling when associated with the MAVS-CARD. Our study provides an alternative model for dsRNA recognition by MDA5 in an ATP- and 2CARD-dependent

manner. The formation of a stable MDA5-RNA complex enables downstream signaling. Future studies will investigate RNA proofreading and the role of LGP2 to further complete our understanding of this essential and conserved innate immune pathway.

Acknowledgments

DD was supported by the Interdisciplinary Center for Clinical Research (IZKF) at the University Hospital of the University of Erlangen-Nuremberg, "BaSyC – Building a Synthetic Cell" Gravitation grant (024.003.019) of the Netherlands Ministry of Education, Culture and Science (OCW) and the Netherlands Organization for Scientific Research (NWO), and the NWO-M Open Competition Domain Science grant (OCENW.M.21.184). YM and RS were supported by the Wellcome Trust (awards 217191/Z/19/Z and 215378/Z/19/Z, respectively). AHdV was supported by the Human Frontier Science Program (fellowship LT000454/2021-L). WHR was supported through the EU INFRAIA consortium MOSBRI. We thank the lab of Annemarthe van der Veen for fruitful discussions.

Data availability

The data of this study are available from the lead authors.

Supplemental Information

Supplemental Information are available online.

Declaration of interest.

YM is a consultant for Related Sciences LLC and has profits interests in Danger Bio LLC. None of the other authors have any conflicts of interest with the content of this article.

Authors Contribution

SQ, YM and DD designed the research. SQ, SM, WHR and DD designed the single-molecule experiments. AHdV, RS and YM expressed and purified recombinant MDA5 proteins. QS and FSP provided the RNA constructs. SQ and SM performed the single-molecule experiments. SQ, SM and PPBA analyzed the data. CPB provided theoretical support. SQ, SM, MK, WHR and DD interpreted the data. YM, SQ and DD wrote the article. All the authors read and edited the article.

Materials and Methods

dsRNA synthesis

A comprehensive protocol for synthesizing dsRNA constructs for magnetic tweezers has been provided in reference (*38*). Briefly, a 3.2 kbp double-stranded RNA (dsRNA) was assembled from single-stranded RNA (ssRNA) oligomers. DNA fragments from pBAD plasmid were amplified using Phusion polymerase with primers (**Table S13**) that contained the T7 promoter. Handles containing Digoxigenin-UTP (Jena Biosciences) or Biotin-UTP (Jena Biosciences) were also amplified to enable attachment to the surface of the flow cell and the magnetic bead, respectively. In vitro transcription was carried out using the HiScribe kit (NEB) to generate ssRNA fragments. If coilability of the tethers was required, the ssRNA fragments were mono-phosphorylated using pyrophosphatase (Thermo Fisher) before annealing and ligated using T4 RNA ligase 2 (NEB). Constructs containing 30 nt gaps, were constructed via shorter ssRNA oligomers for the required strand ('up' or 'down' strand) and annealed to the full-length strand with opposite orientation (**Table S13**).

MDA5 expression and purification.

A detailed protocol of the cloning, expression and purification procedure can be found in (*8*, *9*). MDA5 was cloned into pET28a plasmid with an N-terminal 6x His-tag and TEV protease cleavage site for purification. The MDA5 gene encodes for the mouse *MDA5 (IH1H1)* without residues 646-663 (in this work termed MDA5 WT). Mutants were cloned by overlap PCR. MDA5 WT was expressed in *E.coli* BL21(DE3). The lysate was loaded onto Ni-NTA agarose and eluted using a buffer gradient containing imidazole. After a subsequent anion exchange column, the protein was further purified in a size exclusion chromatography.

Flow cell preparation.

A comprehensive protocol for efficient passivation of flow cells to be used in magnetic tweezers experiments is described in detail in reference (*37*). The top coverslip (#1 24 x 60 mm, Menzel GmbH Germany) were drilled with two holes using a sandblaster (Problast 2, Vaniman USA) and Al_2O_3 particles (34-82 µm, F230, Eisenwerk Wuerth Germany). Both top and bottom coverslips were sonicated in Hellmanex III (Sigma Aldrich) solution (2% V/V in demineralized water) and the bottom coverslip were functionalized by spreading across its surface 4 µl of 1 mg/ml nitrocellulose dissolved in amyl acetate. The flow cell was assembled by sandwiching between a top and bottom coverslip a double layer of Parafilm M with a carved-out channel to connect the two holes of the top coverslip. The flow cell was sealed by melting the Parafilm on a hot plate at 100°C for ~2 min.

As reference beads, either 1.1 µm or 3 µm polystyrene beads (Sigma Aldrich) were used when using either MyOne or M270 Dynabeads (Thermo Fisher) magnetic beads, respectively. To functionalize the flow cell, 50 µl of 50 µg/ml anti-digoxigenin (Roche) was applied and incubated for 30 min. Afterwards, the flow cell was rinsed and flushed with 50 µl of 1 mg/ml BSA (NEB) to prevent non-specific binding of the sample.

The dsRNA tethers were mixed with either 1.1 µm or 3 µm superparamagnetic streptavidin coated beads (MyOne or M270 Dynabeads, Thermo Fisher) and incubated for 5 min before being flushed into the flow cell (*38*, *39*). The unspecific and weakly bound tethers were washed out, and the tethers were further selected for their length and coilability (if applicable).

Magnetic tweezers experiments

The experiments were conducted using a high-throughput magnetic tweezers instrument, which has been previously described in details in references (*34*, *37*, *63–65*).

Briefly, the setup consists of an inverted microscope equipped with a 60x oil immersion objective lens (Nikon Plan APO 60X /1.4 NA Oil) and a CMOS camera (Dalsa Falcon 2 FA-80-12 (12 Mpixel)). The position of the objective can be adjusted using a PIFOC piezo (P-726, Physik Instrumente Germany). An LED (λ=660 nm, 400 mW, LH CP7P, Lumitronix) is used to illuminate the flow cell, which is mounted on top of the objective and equipped with an aspheric condenser lens (ACL25416U-A, ø1", f=16 mm, Thorlabs). Two vertically aligned 5 mm permanent magnets (SuperMagnete, Germany) are mounted on top of the flow cell and can be translated in the z-direction and rotated using linear motors (M-126-PD1 and C-150, respectively, Physik Instrumente Germany) as required. The beads tridimensional position are tracked in real-time using the bead tracker described in reference (*40*). The software and its implementation in LabView are publicly available at https://github.com/jcnossen/qtrk and https://github.com/jcnossen/BeadTracker, respectively. All experiments were performed using a 17 ms shutter time and a 58 Hz acquisition frequency. All time traces presented in this work were filtered by a moving average filter with 58 frames window size.

The MDA5 protein aliquots were stored at a concentration of 1-15.7 µM at -80°C until use. Prior to experiments, the aliquots were thawed and equilibrated at 37°C for 90 minutes. All experiments were conducted in MDA5 measurement buffer (20 mM HEPES, 40 mM sodium chloride, 40 mM potassium chloride, 5 mM magnesium chloride, 2 mM sodium azide, 1 mg/mL BSA, and 1 mM DTT) unless otherwise specified.

We used 3.2 kbp dsRNA to tether the magnetic beads to the flow cell surface. To initiate filament formation, MDA5 and nucleotide were mixed prior to be flushed into the flow cell. Filament formation experiments were performed in the presence of 2 mM ADP at a force of 0.1 pN, unless stated otherwise.

Compaction experiments with pre-assembled MDA5 filaments in the presence of either ADP or AMP-PNP were performed by flushing 200 µl reaction buffer containing ATP into the flow cell after the filament assembly, flushing out excess proteins.

Rotation extension experiments were conducted to determine the coilability of the dsRNA tether at forces of 0.5 pN and 4 pN, with rotations ranging from -50 to +50 turns before the addition of MDA5. After filament formation, the rotation extension was carried out at the indicated force, with rotations ranging from -500 to +500 turns.

High-speed Atomic Force Microscopy

The High-Speed Atomic Force Microscopy (HS-AFM) videos were generated using amplitude modulation tapping mode imaging in liquid (RIBM Japan), using USC-F1.2-k0.15 cantilevers (NanoWorld, Switzerland) with a nominal spring constant of 0.15 N/m and a resonance frequency ≈ 0.6 MHz in liquid (*51*, *66*). All HS-AFM recordings were performed at room temperature and in reaction buffer (20 mM HEPES pH 7.9, 40 mM sodium chloride, 40 mM potassium chloride, 5 mM magnesium chloride, 2 mM sodium azide). The dsRNA (with or without proteins) was incubated using the measurement buffer prior to imaging. A minimal imaging force was maintained by using ~1 nm

cantilever-free amplitude and ~0.8 nm set point amplitude. To follow the MDA5-dsRNA interactions, a mixture of dsRNA, 50 nM MDA5, and 2 mM ADP were prepared 15 minutes prior to surface binding. After incubation of the above-mentioned mixture for 15 minutes on mica, HS-AFM imaging was conducted on a liquid chamber containing 40 µl of measurement buffer. Once a dsRNA-MDA5 complex was localized by HS-AFM imaging, a 10 µl ATP stock was added to the chamber to reach a final ATP concentration of 6 mM. Images were primarily processed using built-in scripts (RIBM, Japan) in Igor Pro (Wavemetrics, Lake Oswego, OR, USA) and analyzed using ImageJ software.

Fitting of force extension data

Force-extension experiments for forces below 8 pN were performed using MyOne magnetic beads and repeated three successive times on each tether before and after the filament has formed and equilibrated. The magnets were lowered at a rate of 0.1 mm/s to progressively increase the force on the tether from 0.1 to 8 pN.

To extract the mechanical properties of the tether, i.e. persistence length L_P and contour length L_C, a non-extensible worm-like chain model (*46*) has been fitted to the individual force-extension trace:

$$F_{RNA}(L_{ext}) = \frac{k_B T}{L_P}\left\{\frac{1}{4(1 - L_{ext}/L_c)^2} - \frac{1}{4} + \frac{L_{ext}}{L_C}\right\} \quad (2)$$

with Boltzmann constant $k_{B,}$ temperature T and tether extension L_{Ext}.

However, large fluctuations caused by Brownian motion can affect the accuracy of position estimation (*41*). To overcome this issue, we integrated the force-extension trace to collapse the Brownian motion onto the function:

$$E(L_{ext}) = \int_0^{L_{ext}} F_{RNA} dL_{ext} = \frac{1}{4}\frac{k_B T L_{ext}^2 (2L_{ext} - 3L_c)}{L_P L_c (L_{ext} - L_c)} \quad (3)$$

We only considered $0\,nm \leq L_P \leq 500\,nm$ and $700\,nm \leq L_C \leq 2000\,nm$ as acceptable fitting results. The mean and standard deviation of L_P and L_C were extracted from fitting the individual traces using **Equation 3**, and used to derive the mean force-extension trace. The worm-like chain model (**Equation 2**) represented in this manuscript use L_P and L_C calculated from **Equation 3**.

Force-extension experiments for forces up to 50 pN were performed using M270 magnetic beads. The individual tethers were stretched from 0.5 pN to 50 pN by moving the magnets towards the flow cell at 0.01 mm/s. The force was subsequently lowered at the same magnets translation rate. Only one cycle on the tether before and after addition of the protein was performed. Rupture forces of compacted MDA5-dsRNA filaments were selected manually from individual traces.

Extracting the filament nucleation, formation and compaction rates

To determine the filament nucleation rate k_{nucl} and pre-compaction rate $k_{pre-comp}$, we manually selected on the 1 Hz low-pass filtered traces the time between the start of the flush of MDA5 in the flow cell and the time where the tether extension increased (**Figure 1C**) or compaction occurred (**Figure 3**).

Concerning filament formation and compaction rates k_{form} and k_{comp}, we first manually selected the regions in the trace where the tether extension either increased or decreased, respectively. k_{form} and k_{comp} were subsequently extracted using a sliding average window of 20 seconds and 50 seconds, respectively, in the selected regions. Only compaction rates larger than 0.1 nm/s (detection limit) were considered. For k_{form}, only increases larger than two times the variance in the trace signal before the MDA5 flush were considered. Filament formation rates were normalized to the footprint of an MDA5 monomer according to

$$\frac{\Delta L_{Ext,300\,nM} \cdot 14\,bp}{3149\,bp} \quad (5),$$

where $\Delta L_{Ext,300\,nM}$ is the change in extension at 0.1 pN upon filament formation with 300 nM WT MDA5 and 2 mM AMP-PNP, 14 bp being the footprint of WT MDA5 and 3149 bp is the length of the dsRNA tethers used in this assay.

For the detection of rupture events during filament compaction (**Figure S4E**), a threshold of twice the standard deviation of the raw signal before addition of ATP was defined. If the extension of the averaged signal crossed this threshold within a 5 second time window, a rupture event was counted.

Fitting the Hill equation on the normalized persistence length L_p

The normalization of the persistence length L_p was performed as described in reference (*48*):

$$\alpha([MDA5]) = \frac{\sqrt{\frac{1}{L_{p,i}}} - \sqrt{\frac{1}{\overline{L_p}}}}{\sqrt{\frac{1}{L_{p,300\,nM}}} - \sqrt{\frac{1}{\overline{L_p}}}} \quad (6)$$

where $\alpha([MDA5])$ is the fractional occupancy of the MDA5-dsRNA filament, $L_{P,i}$ is the persistence length of the filament at a given MDA5 concentration i, $\overline{L_p}$ is the mean persistence length, and $L_{P,300\,nM}$ is the persistence length at 300 nM MDA5. We assume that a complete filament was formed at 300 nM MDA5.

Error estimation for fraction of filament events

We calculated the relative fraction f_{rel} of an event N_i over all events N_{all} and estimated the error δf_{rel} according to

$$f_{rel} = \frac{N_i}{N_{all}}, \quad \delta f_{rel} = \sqrt{\frac{f_{rel}(1 - f_{rel})}{N_{all}}} \quad (7)$$

References

1. F. Weber, V. Wagner, S. B. Rasmussen, R. Hartmann, S. R. Paludan, Double-stranded RNA is produced by positive-strand RNA viruses and DNA viruses but not in detectable amounts by negative-strand RNA viruses. *J Virol* **80**, 5059–5064 (2006).

2. K.-N. Son, Z. Liang, H. L. Lipton, Double-Stranded RNA Is Detected by Immunofluorescence Analysis in RNA and DNA Virus Infections, Including Those by Negative-Stranded RNA Viruses. *J Virol* **89**, 9383–9392 (2015).

3. S. Hur, Double-Stranded RNA Sensors and Modulators in Innate Immunity. *Annu. Rev. Immunol.* **37**, 349–375 (2019).

4. R. de Reuver, J. Maelfait, Novel insights into double-stranded RNA-mediated immunopathology. *Nat Rev Immunol* **24**, 235–249 (2024).

5. Y. G. Chen, S. Hur, Cellular origins of dsRNA, their recognition and consequences. *Nat Rev Mol Cell Biol* **23**, 286–301 (2022).

6. J. Rehwinkel, M. U. Gack, RIG-I-like receptors: their regulation and roles in RNA sensing. *Nat Rev Immunol* **20**, 537–551 (2020).

7. A. G. Dias Junior, N. G. Sampaio, J. Rehwinkel, A Balancing Act: MDA5 in Antiviral Immunity and Autoinflammation. *Trends in microbiology* **27**, 75–85 (2019).

8. Q. Yu, K. Qu, Y. Modis, Cryo-EM Structures of MDA5-dsRNA Filaments at Different Stages of ATP Hydrolysis (2018)pp. 999–10126.

9. Q. Yu, A. Del Herrero Valle, R. Singh, Y. Modis, MDA5 disease variant M854K prevents ATP-dependent structural discrimination of viral and cellular RNA. *Nat Commun* **12**, 6668 (2021).

10. E. Uchikawa, M. Lethier, H. Malet, J. Brunel, D. Gerlier, S. Cusack, Structural Analysis of dsRNA Binding to Anti-viral Pattern Recognition Receptors LGP2 and MDA5. *Mol Cell* **62**, 586–602 (2016).

11. A. Peisley, C. Lin, B. Wu, M. Orme-Johnson, M. Liu, T. Walz, S. Hur, Cooperative assembly and dynamic disassembly of MDA5 filaments for viral dsRNA recognition. *Proc Natl Acad Sci U S A* **108**, 21010–21015 (2011).

12. I. C. Berke, Y. Modis, MDA5 cooperatively forms dimers and ATP-sensitive filaments upon binding double-stranded RNA (2012)pp. 1714–1726.

13. B. Wu, S. Hur, How RIG-I like receptors activate MAVS. *Curr Opin Virol* **12**, 91–8 (2015).

14. B. Wu, A. Peisley, C. Richards, H. Yao, X. Zeng, C. Lin, F. Chu, T. Walz, S. Hur, Structural basis for dsRNA recognition, filament formation, and antiviral signal activation by MDA5. **2**, 276–289 (2013).

15. I. C. Berke, X. Yu, Y. Modis, E. H. Egelman, MDA5 assembles into a polar helical filament on dsRNA (2012)pp. 18437–18441.

16. H. Kato, O. Takeuchi, E. Mikamo-Satoh, R. Hirai, T. Kawai, K. Matsushita, A. Hiiragi, T. S. Dermody, T. Fujita, S. Akira, Length-dependent recognition of double-stranded ribonucleic acids by retinoic acid-inducible gene-I and melanoma differentiation-associated gene 5. *J Exp Med* **205**, 1601–10 (2008).

17. A. Peisley, M. H. Jo, C. Lin, B. Wu, M. Orme-Johnson, T. Walz, S. Hohng, S. Hur, Kinetic mechanism for viral dsRNA length discrimination by MDA5 filaments. *Proc Natl Acad Sci U S A* **109**, 3340–9 (2012).

18. H. Yao, M. Dittmann, A. Peisley, H. H. Hoffmann, R. H. Gilmore, T. Schmidt, J. Schmidt-Burgk, V. Hornung, C. M. Rice, S. Hur, ATP-dependent effector-like functions of RIG-I-like receptors. *Mol Cell* **58**, 541–548 (2015).

19. R. Singh, Y. Wu, A. Del Herrero Valle, K. E. Leigh, S. Mong, M. T. K. Cheng, B. J. Ferguson, Y. Modis, Contrasting functions of ATP hydrolysis by MDA5 and LGP2 in viral RNA sensing. *Journal of Biological Chemistry* **300**, 105711 (2024).

20. X.-P. Han, M. Rao, S.-R. Wu, Q. Zhang, F. Hou, S.-Q. Zhang, L.-L. Chen, J. Liu, *Observation of Higher-Order Assemblies Controlled by Protein One-Dimensional Movement* (2024; https://www.biorxiv.org/content/10.1101/2024.06.06.597732v1.full.pdf).

21. F. Hou, L. Sun, H. Zheng, B. Skaug, Q.-X. Jiang, Z. J. Chen, MAVS forms functional prion-like aggregates to activate and propagate antiviral innate immune response. *Cell* **146**, 448–61 (2011).

22. B. Wu, A. Peisley, D. Tetrault, Z. Li, E. H. Egelman, K. E. Magor, T. Walz, P. A. Penczek, S. Hur, Molecular imprinting as a signal-activation mechanism of the viral RNA sensor RIG-I. *Mol Cell* **55**, 511–23 (2014).

23. H. Kato, O. Takeuchi, S. Sato, M. Yoneyama, M. Yamamoto, K. Matsui, S. Uematsu, A. Jung, T. Kawai, K. J. Ishii, O. Yamaguchi, K. Otsu, T. Tsujimura, C.-S. Koh, C. Reis e Sousa, Y. Matsuura, T. Fujita, S. Akira, Differential roles of MDA5 and RIG-I helicases in the recognition of RNA viruses. *Nature* **441**, 101–5 (2006).

24. D. Kang, R. V. Gopalkrishnan, Q. Wu, E. Jankowsky, A. M. Pyle, P. B. and Fisher, mda-5: An interferon-inducible putative RNA helicase with double-stranded RNA-dependent ATPase activity and melanoma growth-suppressive properties. *BioRxiv* (2002).

25. M. Yoneyama, M. Kikuchi, K. Matsumoto, T. Imaizumi, M. Miyagishi, K. Taira, E. Foy, Y.-M. Loo, M. Gale, S. Akira, S. Yonehara, A. Kato, T. Fujita, Shared and Unique Functions of the DExD/H-Box Helicases RIG-I, MDA5, and LGP2 in Antiviral Innate Immunity. *Journal of immunology (Baltimore, Md. : 1950)* **175**, 2851–2858 (2005).

26. T. Satoh, H. Kato, Y. Kumagai, M. Yoneyama, S. Sato, K. Matsushita, T. Tsujimura, T. Fujita, S. Akira, O. Takeuchi, LGP2 is a positive regulator of RIG-I- and MDA5-mediated antiviral responses. *Proc Natl Acad Sci U S A* **107**, 1512–7 (2010).

27. G. Hartmann, Nucleic Acid Immunity. *Advances in immunology* **133**, 121–169 (2017).

28. F. J. Barrat, K. B. Elkon, K. A. Fitzgerald, Importance of Nucleic Acid Recognition in Inflammation and Autoimmunity. *Annual review of medicine* **67**, 323–36 (2016).

29. H. Oda, K. Nakagawa, J. Abe, T. Awaya, M. Funabiki, A. Hijikata, R. Nishikomori, M. Funatsuka, Y. Ohshima, Y. Sugawara, T. Yasumi, H. Kato, T. Shirai, O. Ohara, T. Fujita, T. Heike, Aicardi-Goutières syndrome is caused by IFIH1 mutations. *American Journal of Human Genetics* **95**, 121–5 (2014).

30. Y. J. Crow, N. Manel, Aicardi-Goutières syndrome and the type I interferonopathies. *Nature reviews. Immunology* **15**, 429–40 (2015).

31. G. I. Rice, Y. del Toro Duany, E. M. Jenkinson, G. M. Forte, B. H. Anderson, G. Ariaudo, B. Bader-Meunier, E. M. Baildam, R. Battini, M. W. Beresford, M. Casarano, M. Chouchane, R. Cimaz, A. E. Collins, N. J. Cordeiro, R. C. Dale, J. E. Davidson, L. Waele, I. Desguerre, L. Faivre, E. Fazzi, B. Isidor, L. Lagae, A. R. Latchman, P. Lebon, C. Li, J. H. Livingston, C. M. Lourenço, M. M. Mancardi, A. Masurel-Paulet, I. B. McInnes, M. P. Menezes, C. Mignot, J. O'Sullivan, S. Orcesi, P. P. Picco, E. Riva, R. A. Robinson, D. Rodriguez, E. Salvatici, C. Scott, M. Szybowska, J. L. Tolmie, A. Vanderver, C. Vanhulle, J. P. Vieira, K. Webb, R. N. Whitney, S. G. Williams, L. A. Wolfe, S. M. Zuberi, S. Hur, Y. J. Crow, Gain-of-function mutations in IFIH1 cause a spectrum of human disease phenotypes associated with upregulated type I interferon signaling. *Nat Genet* **46**, 503–9 (2014).

32. F. Rutsch, M. MacDougall, C. Lu, I. Buers, O. Mamaeva, Y. Nitschke, G. I. Rice, H. Erlandsen, H. G. Kehl, H. Thiele, P. Nürnberg, W. Höhne, Y. J. Crow, A. Feigenbaum, R. C. Hennekam, A specific IFIH1 gain-of-function mutation causes Singleton-Merten syndrome. *American Journal of Human Genetics* **96**, 275–82 (2015).

33. R. Singh, A. Del Herrero Valle, J. Joiner, M. Zwaagstra, B. J. Ferguson, F. J. M. van Kuppeveld, Y. Modis, Molecular basis of pathogenesis and protection from type 1 diabetes by loss of function MDA5 variants. (2024).

34. E. Ostrofet, F. Stal Papini, D. Dulin, Correction-free force calibration for magnetic tweezers experiments. *Scientific Reports* **8** (2018).

35. M. Seifert, P. van Nies, F. Stal-Papini, J. J. Arnold, M. M. Poranen, C. E. Cameron, M. Depken, D. Dulin, Temperature controlled high-throughput magnetic tweezers show striking difference in activation energies of replicating viral RNA-dependent RNA polymerases. *Nucleic Acids Res* **48**, 5591–5602 (2020).

36. D. Dulin, An Introduction to Magnetic Tweezers. *Methods Mol Biol* **2694**, 375–401 (2024).

37. S. Quack, D. Dulin, Surface Functionalization, Nucleic Acid Tether Characterization, and Force Calibration for a Magnetic Tweezers Assay. *Methods Mol Biol* **2694**, 403–420 (2024).

38. F. Stal Papini, M. Seifert, D. Dulin, High-yield fabrication of DNA and RNA constructs for single molecule force and torque spectroscopy. *Nucleic Acids Res* **47** (2019).

39. H. Dohnalová, M. Seifert, E. Matoušková, M. Klein, F. S. Papini, J. Lipfert, D. Dulin, F. Lankaš, Temperature-Dependent Twist of Double-Stranded RNA Probed by Magnetic Tweezer Experiments and Molecular Dynamics Simulations. *The Journal of Physical Chemistry. B* **128**, 664–675 (2024).

40. J. Cnossen, D. Dulin, N. Dekker, An optimized software framework for real-time, high-throughput tracking of spherical beads. *Review of Scientific Instruments* **85** (2014).

41. M. C. . Kruithof, F.-Tso. Chien, Martijn. Jager, J. van Noort, Subpiconewton dynamic force spectroscopy using magnetic tweezers. *Biophys J* **94**, 2343–8 (2008).

42. J. Lipfert, G. M. Skinner, J. M. Keegstra, T. Hensgens, T. Jager, D. Dulin, M. Köber, Z. Yu, S. P. Donkers, F.-C. Chou, R. Das, N. H. Dekker, Double-stranded RNA under force and torque: similarities to and striking differences from double-stranded DNA. *Proc Natl Acad Sci U S A* **111**, 15408–13 (2014).

43. J. Lipfert, M. M. van Oene, M. Lee, F. Pedaci, N. H. Dekker, Torque spectroscopy for the study of rotary motion in biological systems. *Chemical Reviews* **115**, 1449–1474 (2015).

44. T. R. Strick, J. F. Allemand, D. Bensimon, A. Bensimon, V. Croquette, The elasticity of a single supercoiled DNA molecule. *Science (New York, N.Y.)* **271**, 1835–7 (1996).

45. T. van der Heijden, R. Seidel, M. Modesti, R. Kanaar, C. Wyman, C. Dekker, Real-time assembly and disassembly of human RAD51 filaments on individual DNA molecules. 5646–5657 (2007).

46. J. F. Marko, E. D. Siggia, Stretching DNA. *Macromolecules* **28**, 8759–8770 (1995).

47. J. A. Abels, F. Moreno-Herrero, T. van der Heijden, C. Dekker, N. H. Dekker, Single-Molecule Measurements of the Persistence Length of Double-Stranded RNA. **88**, 2737–2744 (2005).

48. J. Chen, S. Le, A. Basu, W. J. Chazin, J. Yan, Mechanochemical regulations of RPA's binding to ssDNA. *Sci Rep* **5**, 9296 (2015).

49. S. Ahmad, X. Mu, F. Yang, E. Greenwald, J. W. Park, E. Jacob, C.-Z. Zhang, S. Hur, Breaching Self-Tolerance to Alu Duplex RNA Underlies MDA5-Mediated Inflammation. *Cell* **172**, 797–81013 (2018).

50. T. Ando, T. Uchihashi, S. Scheuring, Filming biomolecular processes by high-speed atomic force microscopy. *Chemical Reviews* **114**, 3120–3188 (2014).

51. C. van Ewijk, F. Xu, S. Maity, J. Sheng, M. C. A. Stuart, B. L. Feringa, W. H. Roos, Light-Triggered Disassembly of Molecular Motor-based Supramolecular Polymers Revealed by High-Speed AFM. *Angewandte Chemie International Edition* **63**, 202319387 (2024).

52. T. Shigemoto, M. Kageyama, R. Hirai, J. Zheng, M. Yoneyama, T. Fujita, Identification of loss of function mutations in human genes encoding RIG-I and MDA5: implications for resistance to type I diabetes. *Journal of Biological Chemistry* **284**, 13348–54 (2009).

53. C. M. Zerbe, D. J. Mouser, J. L. Cole, Oligomerization of RIG-I and MDA5 2CARD domains. 521–526 (2020).

54. A. Pichlmair, O. Schulz, C. P. Tan, J. Rehwinkel, H. Kato, O. Takeuchi, S. Akira, M. Way, G. Schiavo, C. Reis e Sousa, Activation of MDA5 requires higher-order RNA structures generated during virus infection. *J Virol* **83**, 10761–9 (2009).

55. J.-B. Marq, D. Kolakofsky, D. Garcin, Unpaired 5' ppp-nucleotides, as found in arenavirus double-stranded RNA panhandles, are not recognized by RIG-I. *Journal of Biological Chemistry* **285**, 18208–18216 (2010).

56. K. M. Hastie, C. R. Kimberlin, M. A. Zandonatti, I. J. MacRae, E. O. Saphire, Structure of the Lassa virus nucleoprotein reveals a dsRNA-specific 3' to 5' exonuclease activity essential for immune suppression. *Proc Natl Acad Sci U S A* **108**, 2396–2401 (2011).

57. I. Duic, H. Tadakuma, Y. Harada, R. Yamaue, K. Deguchi, Y. Suzuki, S. H. Yoshimura, H. Kato, K. Takeyasu, T. Fujita, Viral RNA recognition by LGP2 and MDA5, and activation of signaling through step-by-step conformational changes. *Nucleic Acids Res* **48**, 11664–11674 (2020).

58. K.-Y. Lee, C. Craig, S. S. Patel, Unraveling blunt-end RNA binding and ATPase-driven translocation activities of the RIG-I family helicase LGP2. *Nucleic Acids Res* **52**, 355–369 (2024).

59. J. E. Stok, T. Oosenbrug, L. R. Haar, D. Gravekamp, C. P. Bromley, S. Zelenay, C. Reis e Sousa, A. G. van der Veen, RNA sensing via the RIG-I-like receptor LGP2 is essential for the induction of a type I IFN response in ADAR1 deficiency. *The EMBO Journal* **41**, 109760 (2022).

60. N. Gillich, Z. Zhang, M. Binder, S. Urban, R. Bartenschlager, Effect of variants in LGP2 on MDA5-mediated activation of interferon response and suppression of hepatitis D virus replication. *Journal of Hepatology* **78**, 78–89 (2023).

61. A. M. Bruns, G. P. Leser, R. A. Lamb, C. M. Horvath, The innate immune sensor LGP2 activates antiviral signaling by regulating MDA5-RNA interaction and filament assembly. *Mol Cell* **55**, 771–81 (2014).

62. S. Deddouche, D. Goubau, J. Rehwinkel, P. Chakravarty, S. Begum, P. V. Maillard, A. Borg, N. Matthews, Q. Feng, F. J. M. van Kuppeveld, C. Reis e Sousa, Identification of an LGP2-associated MDA5 agonist in picornavirus-infected cells. *Elife* **3**, 01535 (2014).

63. D. Dulin, T. J. Cui, J. Cnossen, M. W. Docter, J. Lipfert, N. Dekker, High Spatiotemporal-Resolution Magnetic Tweezers : Calibration and Applications for DNA Dynamics. *Biophysical Journal* **109**, 2113–2125 (2015).

64. E. Ostrofet, F. Stal Papini, D. Dulin, High spatiotemporal resolution data from a custom magnetic tweezers instrument. *Data Brief* **30** (2020).

65. D. Dulin, S. Barland, X. Hachair, F. Pedaci, Efficient Illumination for Microsecond Tracking Microscopy. *PLoS One* **9**, 107335 (2014).

66. S. Maity, G. Trinco, P. Buzón, Z. R. Anshari, N. Kodera, K. X. Ngo, T. Ando, D. J. Slotboom, W. H. Roos, High-speed atomic force microscopy reveals a three-state elevator mechanism in the citrate transporter CitS. *Proc. Natl. Acad. Sci. U.S.A.* **119**, 2113927119 (2022).

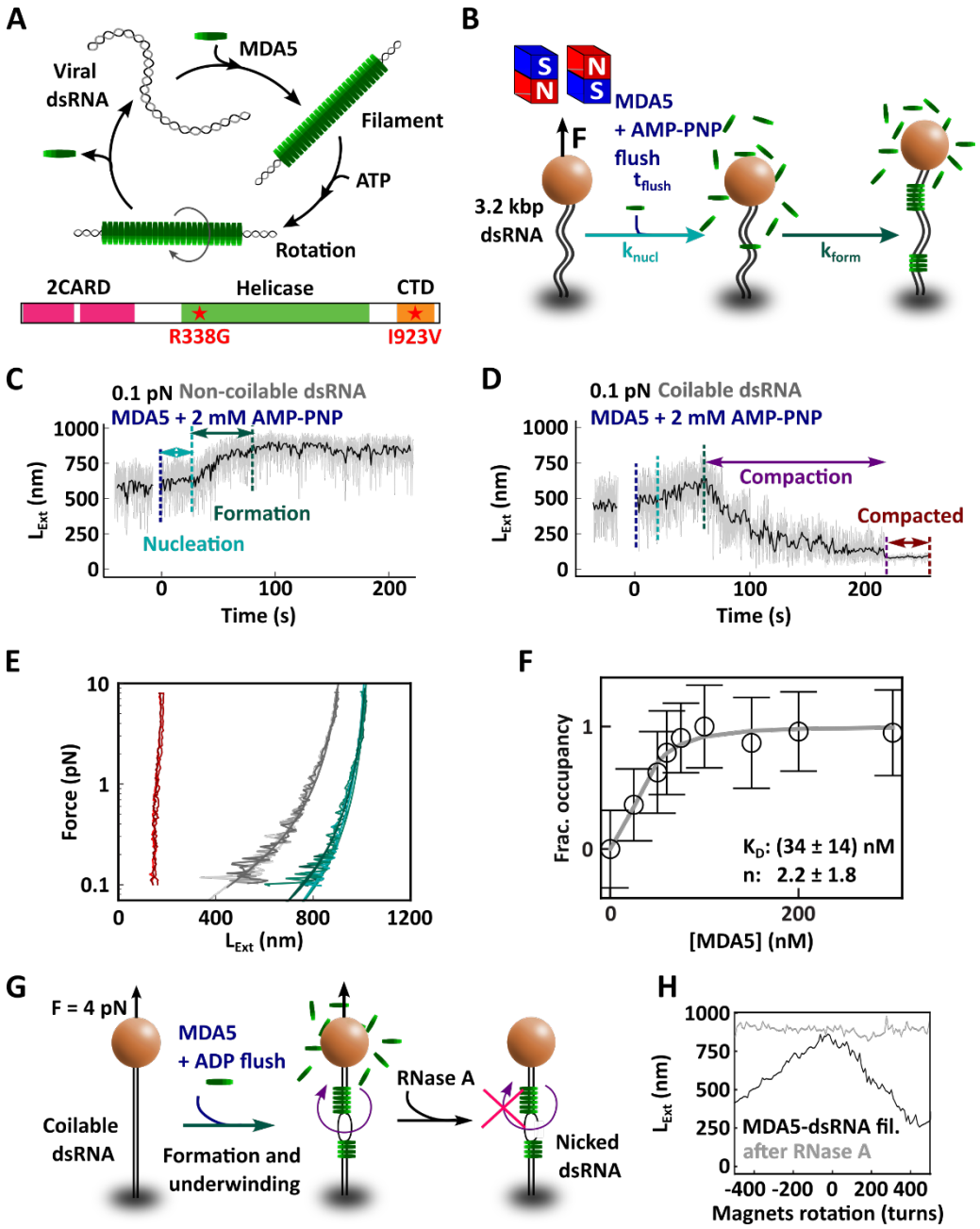

Figure 1: MDA5 assembles cooperatively on long dsRNA in the presence of either ADP or AMP-PNP to form stable and stiff filaments. (A) Schematic of the current model of MDA5-RNA activation and of the different domains composing MDA5. MDA5 (green disk) recognizes viral dsRNA (grey) and cooperatively assembles into filaments. Upon ATP hydrolysis, MDA5 monomers rotate and can subsequently dissociate from the dsRNA. Dynamic assembly and disassembly select for long dsRNA. **(B)** Schematic of the magnetic tweezers assay to monitor MDA5 filament formation. **(C, D)** Time trace of MDA5 filament formation with 100 nM MDA5 and 2 mM AMP-PNP on either **(C)** a non-coilable 3.2 kbp dsRNA or **(D)** a coilable 3.2 kbp dsRNA tether, respectively, as illustrated in (B) (grey). The vertical dashed lines indicate the end of each phase: flushing of MDA5 with AMP-PNP (blue), nucleation (teal) and filament formation (green). The raw (58 Hz) and time averaged (1 Hz) traces are represented in grey and black, respectively. **(E)** Three repetitions of force-extension experiments on either a dsRNA tether (grey), a MDA5 filament in the presence of AMP-PNP on non-coilable dsRNA (green), or a coilable dsRNA (red), respectively. The solid lines are worm-like chain model fits to the data (**Equation 2**, **Materials and Methods**). **(F)** Fractional occupancy (black circles) of MDA5-dsRNA filament according to **Equation 6** fitted with a Hill fit (black line) to obtain the K_D and the Hill coefficient n (**Equation 1**). The error bars are one standard deviation calculated using error propagation. **(G)** Description of the experiment demonstrating dsRNA

underwinding upon MDA5 binding. The MDA5 filament was assembled on a coilable tether, at 4 pN force, in the presence of ADP and with the magnets clamping the magnetic bead in rotation. Excess of MDA5 was then flushed out and RNase A injected in the flow cell. Rotation-extension experiment was subsequently performed to determine tether coilability. **(H)** Rotation extension curve of a coilable MDA5-dsRNA filament before (black) and after RNase A treatment (grey) as described in (G).

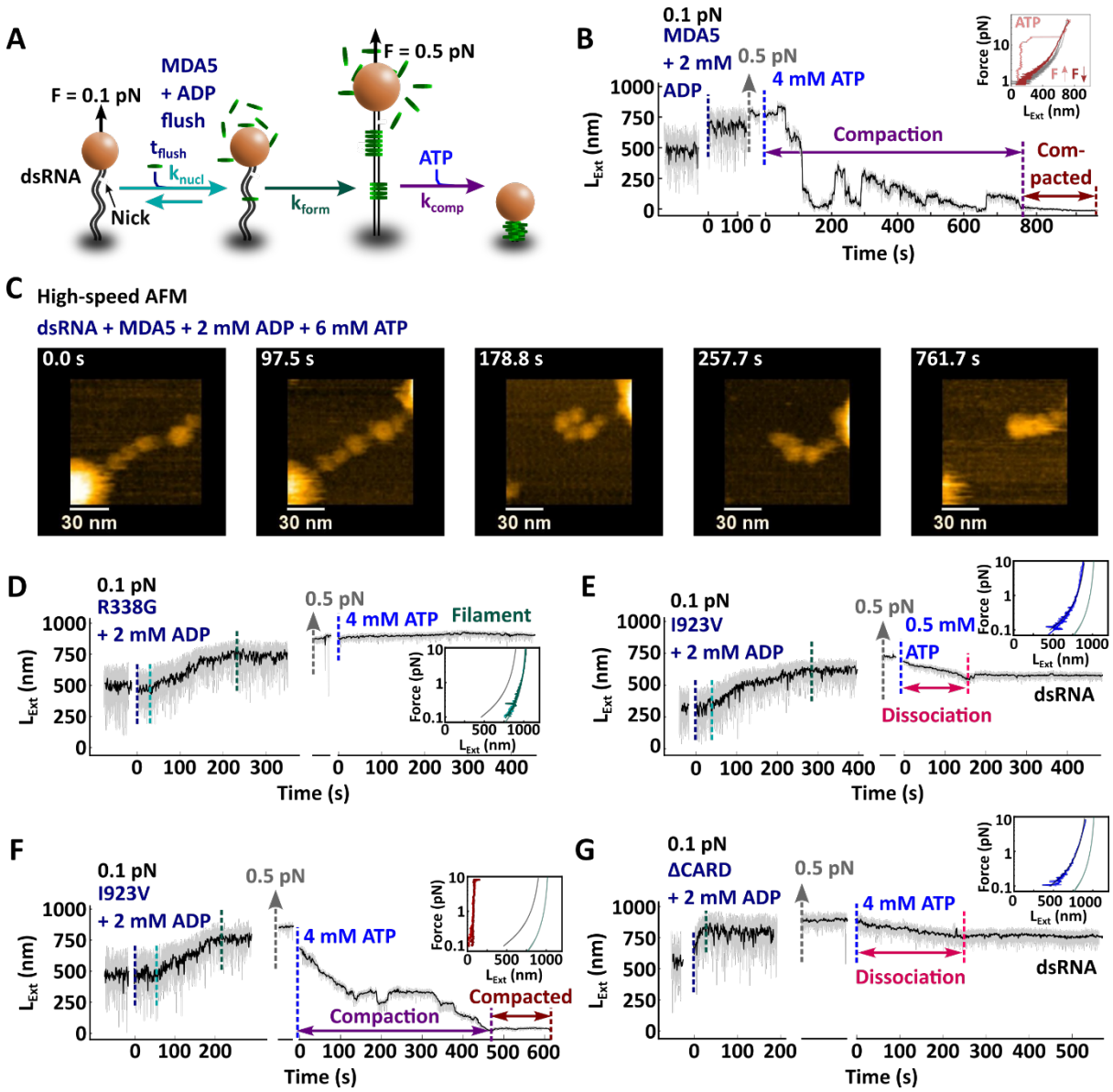

Figure 2: MDA5 filament compaction is ATP-hydrolysis dependent and CARD-CARD interactions are essential to tighten the MDA5-RNA complex. (A) Description of the experiment monitoring the filament formation upon injection of 100 nM MDA5 with 2 mM ADP at 0.1 pN force, followed by a force increase to 0.5 pN and a reaction buffer containing 4 mM ATP addition, which removed the MDA5 proteins in excess. **(B)** Time trace of the filament formation and compaction for the experiment described in (A). The vertical dashed lines indicate the end of each phase: flushing (dark blue), nucleation (turquoise), filament formation (teal), filament compaction (purple) and compacted filament (dark red). The raw (58 Hz) and time averaged (1 Hz) traces are represented in grey and black, respectively. Inset: force-extension of a bare dsRNA tether (grey), and a compacted MDA5 filament when increasing (light red) and subsequently decreasing force (dark red). **(C)** Snapshots of HS-AFM video (**Video S1**) of a complex of dsRNA and 50 nM MDA5 after addition of 6 mM ATP (time reset to 0 s). The dsRNA-MDA5 complex was obtained in the presence of 2 mM ADP (**Figure S4FG**). Imaging rate 300 milliseconds per frame. **(D)** Time trace of the filament formation with MDA5 R338G as described in (A, B). **(E, F)** Time trace of the filament formation with MDA5 I923V as described in (A, B), with addition of either **(E)** 0.5 mM ATP or **(F)** 4 mM ATP. **(G)** Time trace of the filament formation with MDA5 ΔCARD as described in (A, B). Inset in (D, E, F, G): force-extension traces of MDA5 filament after addition of ATP, resulting in either no compaction (green), full compaction (red) or dissociation (blue). Non-extensible WLC fits to force-extension experiments for dsRNA (grey line) and MDA5 filament (teal line). Statistics and WLC fits parameters values are provided in **Table S7**.

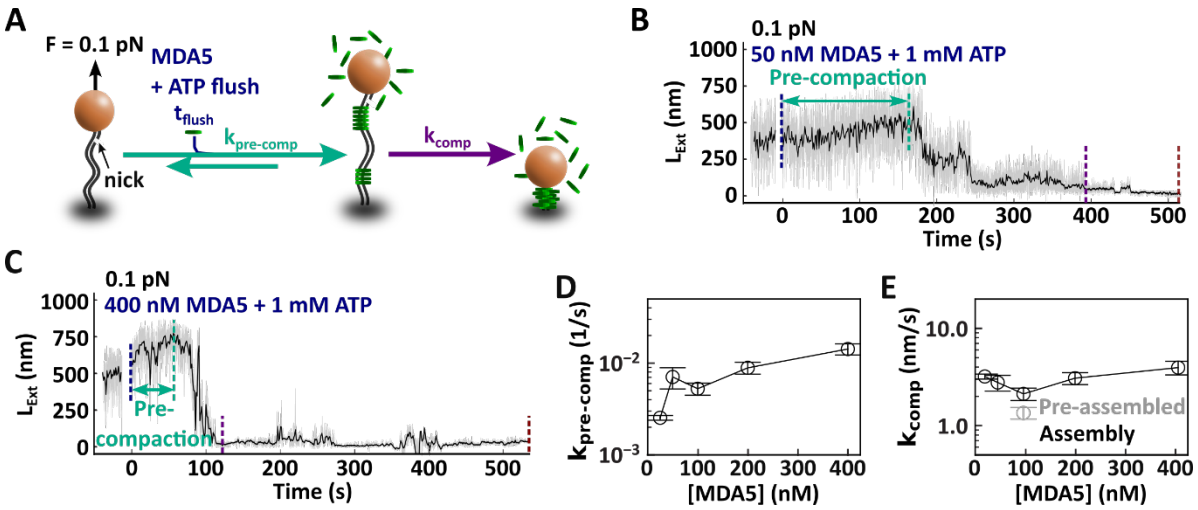

Figure 3: Complete MDA5 filament formation is not required for compaction to occur. (A) Description of the experiment monitoring the filament formation upon the direct injection of MDA5 with 1 mM ATP. **(B, C)** Time trace of the filament formation with **(B)** 50 nM or **(C)** 400 nM MDA5 and compaction for the experiment described in (A) at 0.1 pN. The vertical dashed lines indicate the end of each phase: flushing (dark blue), pre-compaction (teal), compaction (purple) and the compacted filament (dark red). The raw (58 Hz) and time averaged (1 Hz) traces are represented in grey and black, respectively. **(D)** Mean pre-compaction rate of MDA5 on dsRNA in the presence of 1 mM ATP. **(E)** Mean compaction rate of MDA5 filaments at 0.1 pN formed in presence of 1 mM ATP (black) or pre-assembled with 2 mM ADP and subsequent addition of 1 mM ATP (grey). (D, E) The error bars represent standard deviation from 1000 bootstraps. Lines are guide for the eye. Statistics, mean, and error values are provided in **Table S1, Table S6** and **Table S8**.

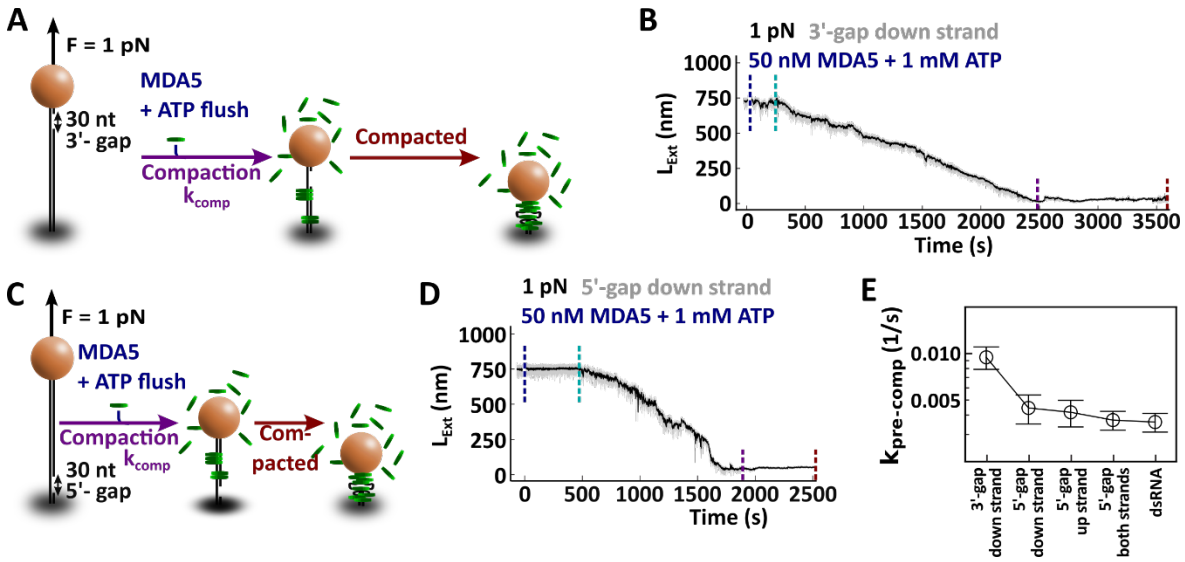

Figure 4: MDA5 preferentially loads on dsRNA via a recessed 3'-end. (A, B) Description of MDA5 filament formation and compaction in the presence of ATP and low MDA5 concentration when using either a **(A)** 3'-gap or **(B)** a 5'-gap construct, respectively. **(C, D)** Tether extension as a function of time for the experiments described in (A, B). **(E)** Mean pre-compaction rates of MDA5 for the dsRNA constructs described in the legend in the presence of 1 mM ATP at 1 pN force. The error bars represent one standard deviation from 1000 bootstraps. Statistics, mean, and error values are provided in **Table S10**.

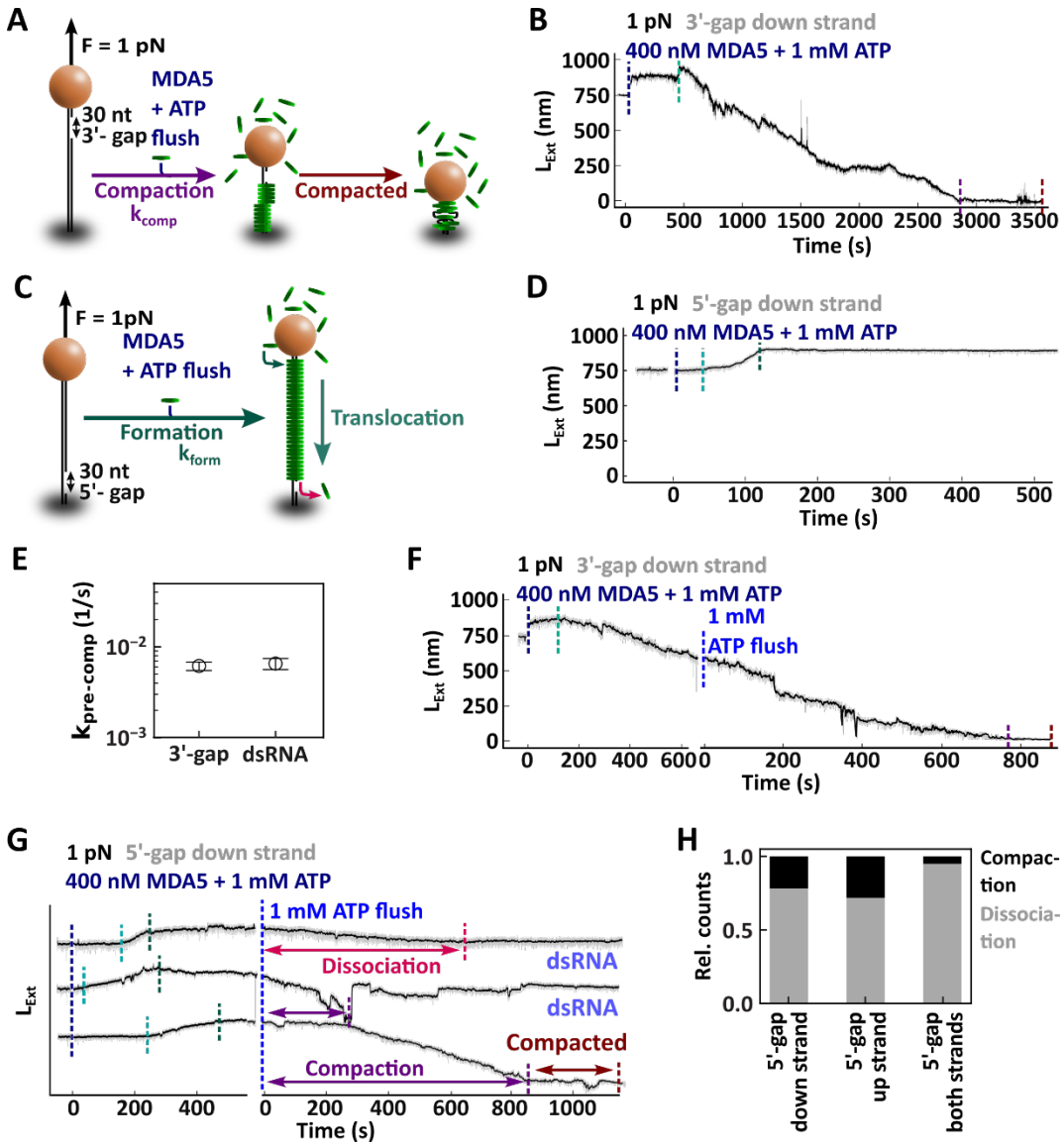

Figure 5: MDA5 translocates 3' to 5' and dissociates by running off the 5'-end. (A, C) Description of the experiment to monitor filament formation with 400 nM MDA5 and 1 mM ATP on dsRNA construct with either **(A)** a 3'-gap or **(C)** a 5'-gap. **(B, D)** Time traces for the experiments described in (A, C), respectively. **(E)** Mean pre-compaction rates of MDA5 3'-gap and dsRNA constructs in the presence of 1 mM ATP. The error bars represent one standard deviation from 1000 bootstraps. Statistics, mean, and error values are provided in **Table S10**. **(F, G)** Time traces of filament formation with 400 nM MDA5 and 1 mM ATP at 1 pN on an dsRNA construct with either (F) a 3'-gap or (G) a 5'-gap. The free proteins were flushed out after 600 s with a buffer containing 1 mM ATP. The three traces in (G) show (top) MDA5 dissociation, (middle) partial compaction before dissociation and (bottom) full compaction of the filament. **(H)** Relative fraction of MDA5 filaments that dissociate versus compact after flushing out the free MDA5 with a buffer containing 1 mM ATP. Three constructs with a 5'-gap at either or both RNA strands were evaluated.

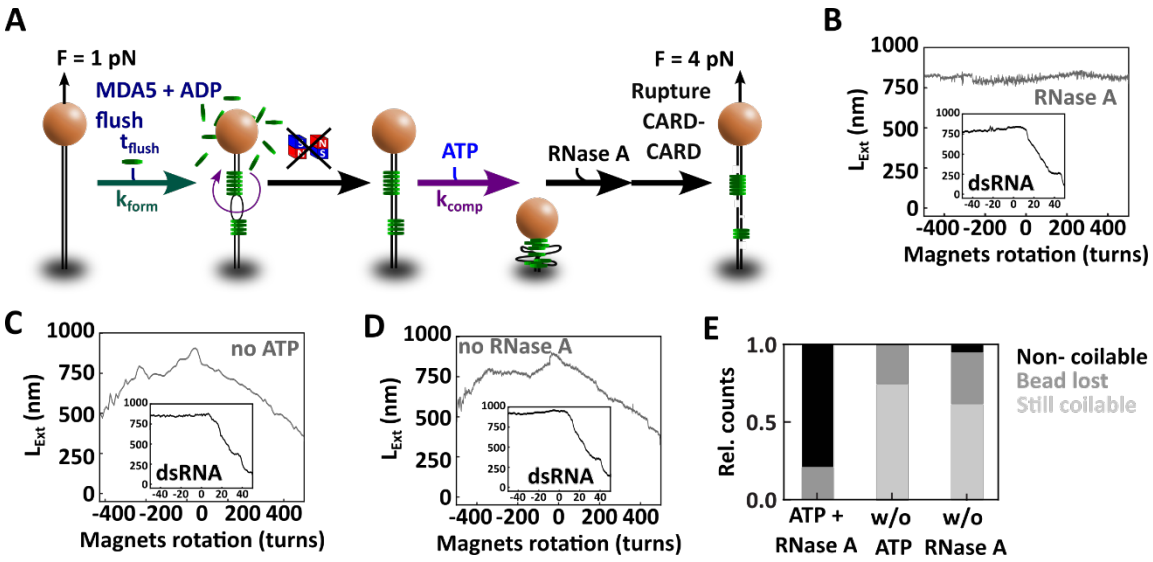

Figure 6: MDA5-RNA complex compaction results from ATP-dependent dsRNA unwinding and single-stranded RNA loops extrusion. (A) Schematic of the experiment reporting on ssRNA loop extrusion by MDA5. The filament was formed on a coilable dsRNA with 100 nM MDA5 and 2 mM ADP, the magnets were removed at the end of the assembly to let any torsional stress relax. The free proteins were then flushed out with a reaction buffer containing 4 mM ATP, which led to compaction. Once the MDA5-RNA complex had compacted, RNase A was added to the compacted MDA5-RNA complex. The magnets were added back and high force was applied to break apart the MDA5-RNA complex. A rotation-extension experiment was subsequently performed to evaluate the coilability of the tether. **(B, C, D)** Rotation-extension of an initially coilable dsRNA **(B)** after performing the treatment as described in (A), **(C)** without the ATP addition step described in (A) and **(D)** without the RNase A step described in (A). The insets report on the coilability of the dsRNA at the start of the experiment. **(E)** Relative count of coilable dsRNA that are no longer coilable (black), lost (grey), or still coilable (light grey) at the end of the experiments represented in (B, C, D). Statistics provided in **Tables S12**.

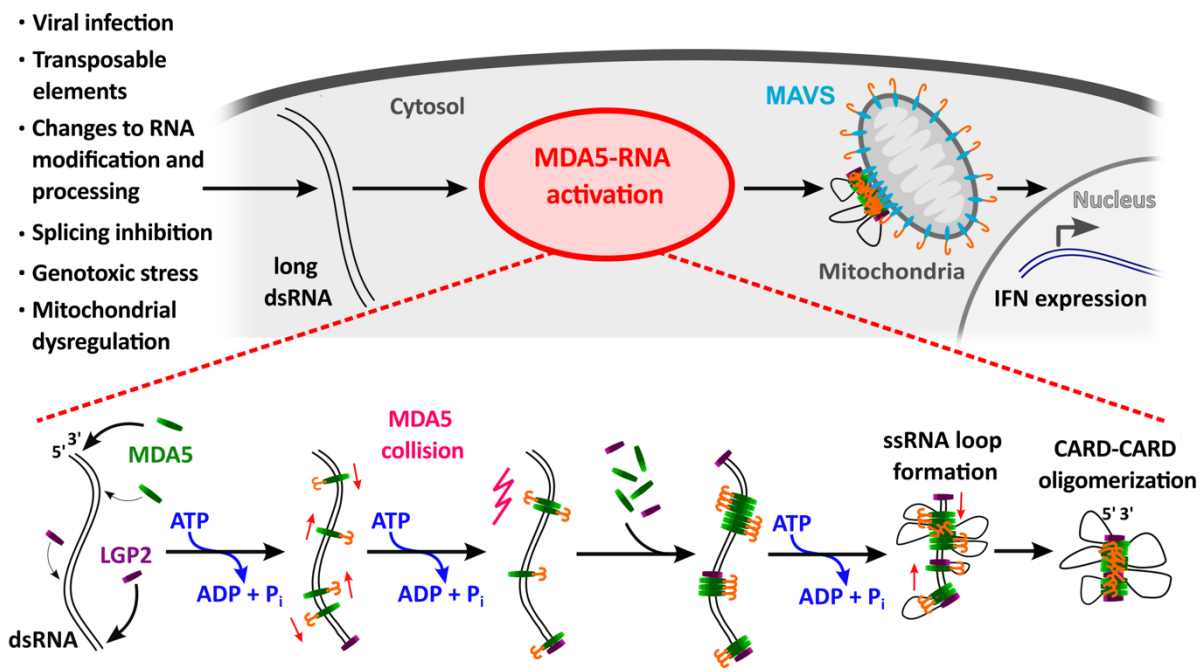

Figure 7: Mechanism of MDA5 activation by dsRNA. The presence of long dsRNA in the cytosol is related to many cellular dysfunctions and viral infections, and induces MDA5 activation *(5)*. MDA5 rapidly loads onto the dsRNA, preferably through the 3'-end at low MDA5 concentration and employs ATP hydrolysis to translocate 3' to 5' along the dsRNA. Eventually, MDA5 collides with either another MDA5 translocating on the opposite strand, or a LGP2 bound either internally or at one of the dsRNA ends. MDA5s cumulate at the collision point, forming a partial filament, which then extrudes ssRNA loops to form a tightly compacted MDA5-RNA complex. This complex is stabilized by CARD-CARD oligomerization, preventing MDA5 dissociation and thereby any future usage of the dsRNA for viral replication or transcription. Finally, the compacted MDA5-RNA complex can associate with the MAVS CARD to enable further signaling towards interferon (IFN) expression.